Ru-Dye Grafted CuS and Reduced Graphene Oxide (CuS/rGO) Composite: An Efficient and Photo Tunable Electrode for Dye Sensitized Solar Cells

K. K. Saravanan & P. SivaKarthik

Journal of Cluster Science
Including Nanoclusters and Nanoparticles

ISSN 1040-7278
Volume 31
Number 2

J Clust Sci (2020) 31:401-407
DOI 10.1007/s10876-019-01653-1

Springer

Journal of Cluster Science (2020) 31:401–407
https://doi.org/10.1007/s10876-019-01653-1

ORIGINAL PAPER

Ru-Dye Grafted CuS and Reduced Graphene Oxide (CuS/rGO) Composite: An Efficient and Photo Tunable Electrode for Dye Sensitized Solar Cells

K. K. Saravanan[1] · P. SivaKarthik[2]

Received: 23 June 2019 / Published online: 12 August 2019

Abstract
The CuS@reduced graphene oxide (CuS/RGO) hybrid nanocomposite was synthesized by facile hydrothermal method and used as a photoelectrode material in photovoltaic applications. In the hydrothermal route, RGO is formed by the reduction of GO with simultaneous formation of CuS/RGO nanocomposites. The CuS/RGO nanocomposites was investigated using powder XRD, TEM, HR-TEM, Raman, XPS, DRS UV–Vis spectroscopy, Photoluminescence (PL) measurements. XRD and TEM results suggest that CuS crystalline with individual spherical like homogeneous nanoparticles sizes in the range of 45–35 nm, which is distributed throughout the RGO sheets. We further construct the flexible photoelectrodes by using CuS and RGO and studied the photovoltaic performance. Photovoltaic parameters, such as short-circuit photocurrent density, open circuit voltage, fill factor and conversion efficiency were found to be 16 mA/cm^2, 0.71 V, 70.1% and 7.81% respectively, for CuS/RGO photoelectrode. The improved photo conversion efficiency of CuS/RGO is due to enhancing the electronic injection ability and reducing the photogenerated charge recombination. These photovoltaic results indicate a simple methodology for the low cost and effortless synthesis of an alternative CuS/RGO photoelectrode in high performance photovoltaic devices.

Keywords CuS · Reduced graphene oxide · Composites · Photovoltaic cell · Energy conversion

Introduction

The diminishing accessibility of fossil fuels, which represent over 80% of the world's vitality utilize, manages a critical move toward renewable energy sources [1–3]. In this situation, sun based energy is considered as a promising innovation, due to its accessibility and wealth. Such exponential increment in energy utilization additionally a rapidly expanding world populace has developed as a challenge to fulfill energy requests; more importantly in a cost-effective and environment friendly way. Within the same setting, energy efficient technologies, such as photovoltaics, water splitting, hydrogen fuel era, attractive refrigeration, and thermoelectricity etc. have been broadly examined for the advancement of elective and/or renewable vitality advances. Among different innovations, photovoltaics has picked up an emerging status owing to its coordinate part within the energy transformation process, differences of materials and/or plans for devices [4–12]. Many researchers have studies different kinds of semiconducting lead chalcogenides such as Cu_2S [13], CoS [14], NiS [15], PbS [16], and noble metals (Au, Pt and so on) in order to improve the photovoltaic efficiency. Among them, CuS is a metal chalcogenide and an significant p-type semiconducting material and huge range of applications and exclusive chemical, physical, optical and electronic properties [17, 18], which has been broadly considered for a variety of applications such as photocatalysis, solar cells, electro-chemistry, catalyst, super ionic materials and Li-ion batteries [19–21].

However, CuS has a comparatively low conductivity, and huge volume variation amid charge/discharge process

✉ P. SivaKarthik
psivakarthick@yahoo.com

[1] Department of Electrical and Electronics Engineering, University College of Engineering, Thirukkuvalai, Tamilnadu 610 204, India

[2] Department of Chemistry, University College of Engineering, Panruti, Tamilnadu 607 106, India

this become a difficulty to the promising application for photovoltaic. Hence, it is enviable to combine CuS with high electrical conductivity carbon material such as graphene to improve the charge transfer, and realize the exploitation as photoelectrode material [22, 23]. Most of the literature focuses on the metal oxide based composites with graphene sheets, only few reports to chalcogenide-based nanocomposites for photovoltaic applications. Hence, we report the high performance photo conversion efficiency of sandwich type CuS/RGO photoelectrode for this work. To the best of the author's awareness, this is the first report about high performance photovoltaic applications of hybrid CuS/RGO photoelectrode by one step hydrothermal route.

Materials and Methods

Materials

Copper nitrate ($Cu(NO_3)_2$), thiourea (CH_4N_2S) and graphite purchased from Sigma-Aldrich, purity 99.99% (Japan) and were utilized as gotten without advance refinement. Fluorine doped tin oxide (FTO) conducting glass substrates were bought from Hind High Vacuum (HHV). The glass wares were washed systematically and dried in hot air oven previous to use.

Preparation of rGO and CuS/rGO Nanocomposite

GO was synthesized by the modified Hummers' method [24], and the CuS/rGO composites were synthesized via a hydrothermal method, using $Cu(NO_3)_2$ as oxidizer and thiourea as fuel, respectively. In the preparation of CuS/RGO, 1 mmol of copper nitrate was added in 50 mL of DI and the solution was stirred incessantly. When a blue solution had formed, 3 mmol of thiourea was directly added. Once the solution was well isolated, 50 mg of RGO was added to the mixture and stirred for 30 min. Then the black color precipitate was transferred into a 100 mL Teflon-lined autoclave, which was then kept at 180 °C for 12 h. After cooled to the room temperature, the precipitate was cleaned with water and ethanol, respectively, and then dried at 60 °C for 12 h. This final product was marked as RGO, CuS and CuS/RGO.

Characterization Techniques

XRD patterns of the synthesized samples were recorded by Bruker D8 Progress using Cu-Kλ as the radiation source (wavelength: 1.54056 Å). Microstructure investigation was performed by a JEOL JEM 2100F high-resolution transmission electronic magnifying instrument (HRTEM). DRS measurements were carried out employing a Hitachi UV-365 spectrophotometer prepared with an coordination circle connection with the wavelength ranges from 300 to 700 nm. The elemental vibration modes of the tests were measured by utilizing Raman spectra of the tests were recorded utilizing BRUKER RFS 27: Stand alone FT-Raman Spectrometer at a determination of 0.2 cm^{-1}. The specific surface areas and porous nature of materials were further investigated by nitrogen adsorption/desorption measurements on nova 2200e. X-ray photoelectron spectrum (XPS) was analyzed by using a Thermo Scientific K-alpha surface analysis instrument.

Fabrication of Photoanode

FTO-coated glass with dimensions of 2.5 × 2.5 cm^2 was used as substrate. Prior to the deposition, the substrate was cleaned ultrasonically within acetone, methanol, and deionized water (DI water, 18.20 MΩ cm) for 5 min each. CuS and CuS/rGO were synthesized to fabricate the photoanode of the DSSC. Initially, CuS and rGO was synthesized by using a hydrothermal process. Then, the FTO substrate was placed into the autoclave and then loaded into the oven at 200 °C for 4 h. The sample was rinsed with DI water after being cooled down naturally to room temperature. Then, the sample was naturally dried in air at room temperature. Finally, the photoanodes were sensitized under dark conditions using an ethanol solution containing the N719 dye (0.01 g of N719 in 20 mL of ethanol) for 24 h.

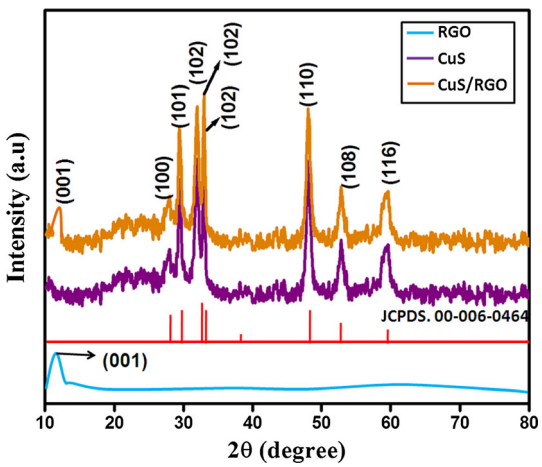

Fig. 1 Powder X-ray diffraction pattern of pure RGO, CuS and CuS/RGO composite samples

Results and Discussion

Figure 1 shows the powder XRD pattern of bare RGO, CuS and CuS/RGO samples respectively. As shown in Fig. 1, the XRD pattern of GO exhibited a peak at 11.4° which was assigned to the (001) reflection of RGO [25]. In bare CuS, the diffraction peaks at the 2θ values of 27.5°, 27.4°, 29.8°, 31.5°, 32.6°, 48.1°, 52.4° and 59.8°, which are assigned to (100), (101), (102), (103), (106), (110), (108) and (116) planes of CuS crystal. The typical peaks were good agree with the hexagonal plane of CuS (JCPDS no. 00-006-0464). Whereas, there is no changes in the peak position of CuS/RGO, the coexistence of (001) plane diffraction peak (2θ = 11.5°) from carbon structure and CuS characteristic peaks indicated the CuS/RGO composite was assorted without phase transformation. Moreover, this peak intensity was decreased than compared with bare CuS. The average grain size was also confirmed by using the Debye-Scherer's equation [26]. The grain size was found to be 42, 38 and 29 nm for RGO, CuS, and CuS/RGO samples respectively. TEM and HRTEM images were carried out to know the surface morphology of the samples. Figure 2 shows the TEM images of pristine RGO, CuS and RGO/CuS. The TEM image of bare RGO is found that the randomly aggregated, wrinkled RGO sheets loosely packed together (Fig. 2a). The TEM image of pure CuS is clearly visible that homogeneous individual spherical shaped morphology with 45–35 nm size (Fig. 2b). The crystal structure of CuS was confirmed by the high resolution TEM (HRTEM), as shown in Fig. 2c. The clear lattice fringes in the HRTEM image confirms that crystalline nature of CuS, and obvious lattice fringes with the 3.05 and 3.24 Å corresponding to (102) and (101) planes of hexagonal CuS. Figure 2d shows the TEM image of CuS/RGO nanocomposite. It was clear evident that individual spherical nanoparticles (35–30 nm) were uniformly wrapped on the surface of the RGO nanosheets. Further authenticate the CuS/RGO nanocomposite, elemental composition analysis was carried out. Figure 2e, f shows the EDS graph of pure CuS and CuS/RGO samples, respectively. The spectra mainly exhibit Cu, S and C elements. The presence of C element in the CuS/RGO sample confirms that formation of CuS/rGO nanocomposites. Figure 3 shows the Raman spectra of the samples. As

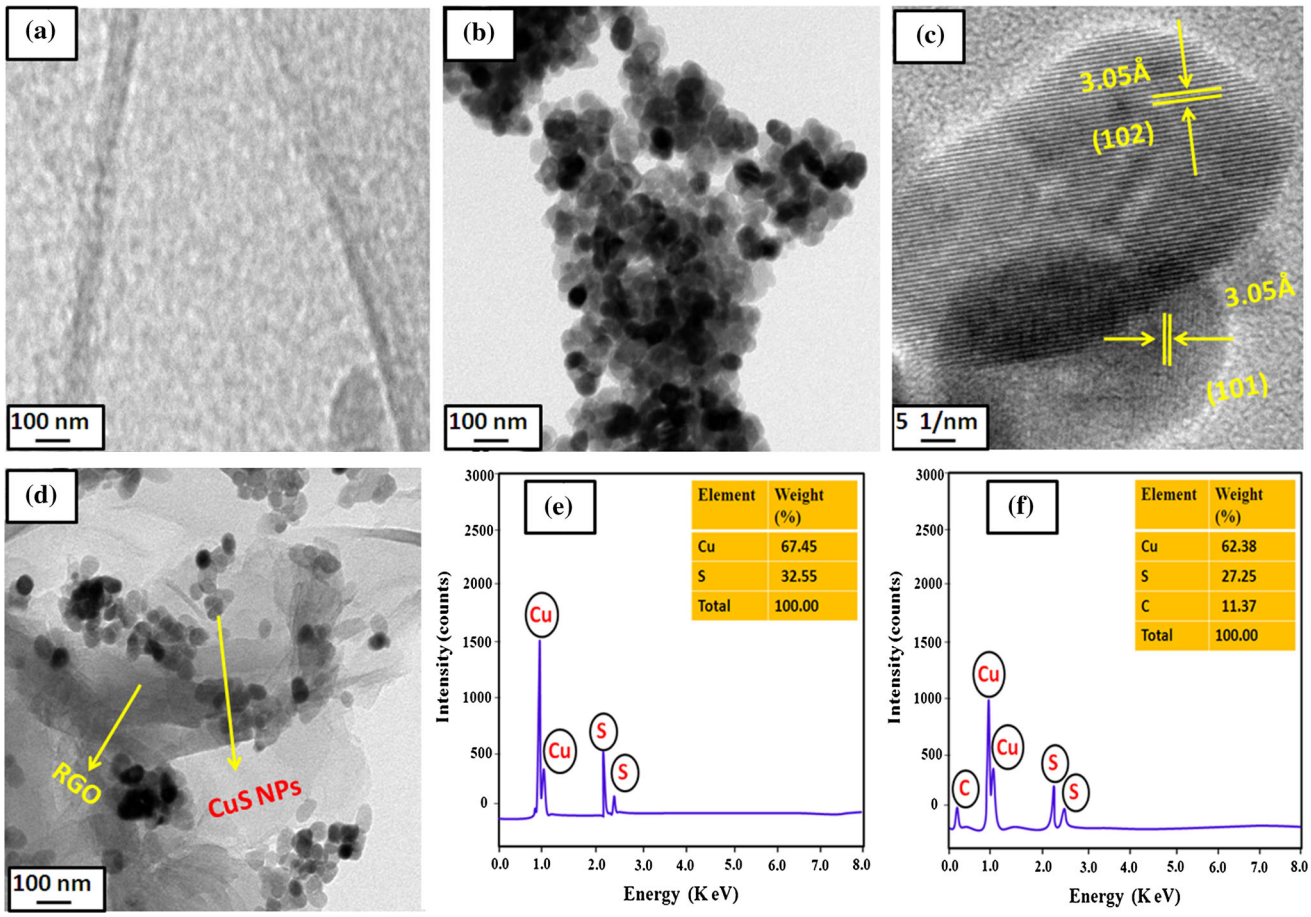

Fig. 2 TEM images of **a** RGO; **b** CuS; **c** HRTEM image of CuS; **d** TEM image of CuS/RGO; **e**, **f** EDS images of pure CuS and CuS/RGO samples respectively

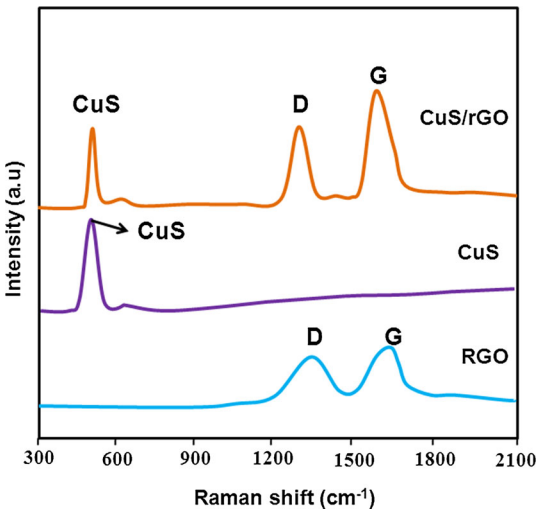

Fig. 3 Raman spectra of bare RGO, CuS and CuS/RGO composite samples

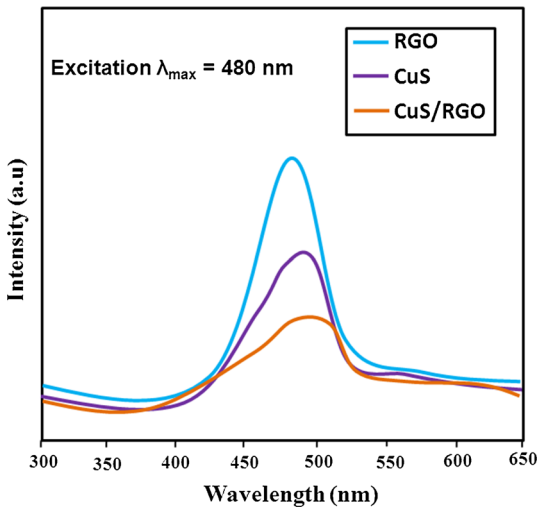

Fig. 5 Photoluminescence spectra of pure RGO, CuS and CuS/rGO composite samples

shown in Fig. 3, there are two bands appeared at 1358 and 1598 m^{-1} in the bare RGO, which is belongs to D and G bands of hexagonal graphitic layer [27, 28]. These bands are due to disarray and defects and sp^2 bonded carbon atoms obtained in the hexagonal graphitic layer. The Raman spectrum of CuS is located at 475 cm^{-1}, which belongs to A_{1g} mode of CuS. The presence of CuS peak mode along with D and G bands in the CuS/RGO composite, further confirming the successful assembly between CuS and RGO. Figure 4a shows the UV-DRS spectra of the RGO, CuS and CuS/RGO samples. The absorption edge of bare RGO and CuS was found to be 460 and 480 nm, further these bands were transferred to higher wavelength region and these results indicate that decreasing the band gap of CuS/RGO. Using the Kubelka–Munk (K–M) model [29], the band gap energy of the samples was calculated by based on the absorption values [30]. The finding band gap energies were 2.69, 2.57 and 2.27 eV for bare RGO, CuS and CuS/RGO sample respectively (Fig. 4b). The photoluminescence spectrum of CuS and CuS/RGO composites is shown in Fig. 5. The excitation wavelength of 400 nm has been used by Xe lamp as laser source. The broad emission peak appeared at 480 nm in all the three cases. There is no change in the peak position but slight variation is observed in the intensity of peaks. This could be due to the size effect of CuS [31]. The precise surface area and porosity of the CuS and CuS/RGO samples were explored by using N_2 adsorption–desorption isotherms, as shown in Fig. 6a. The curve clearly demonstrates that both samples showed characteristic hysteresis loop owing to the subsistence of mesoporous structure [32]. The BET surface area and pores size of the CuS/RGO samples were calculated to

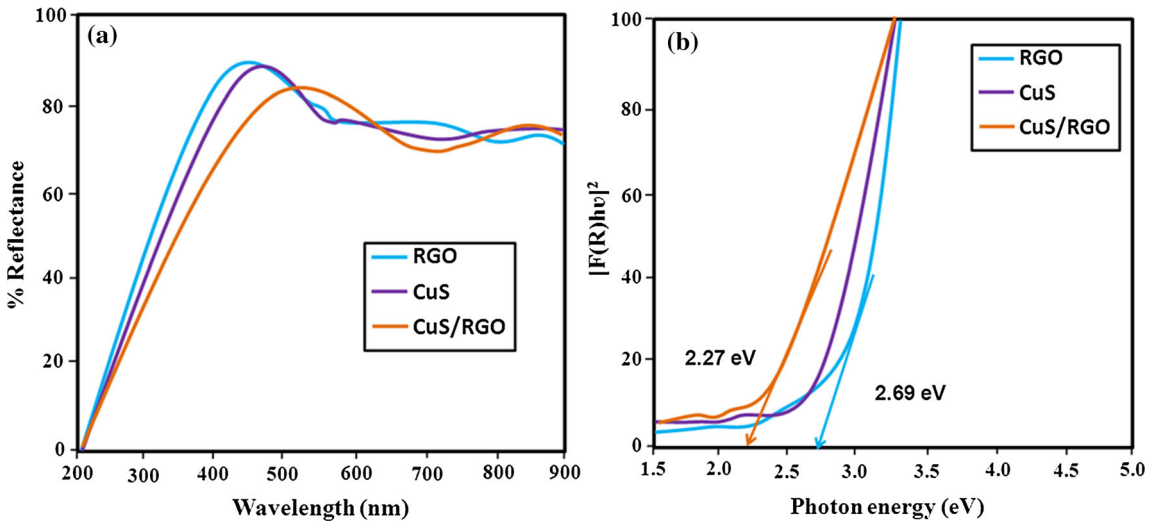

Fig. 4 UV–Vis DRS spectra of pure RGO, CuS and CuS/rGO composite samples. **a** Reflectance spectra. **b** Kubelka–Munk model

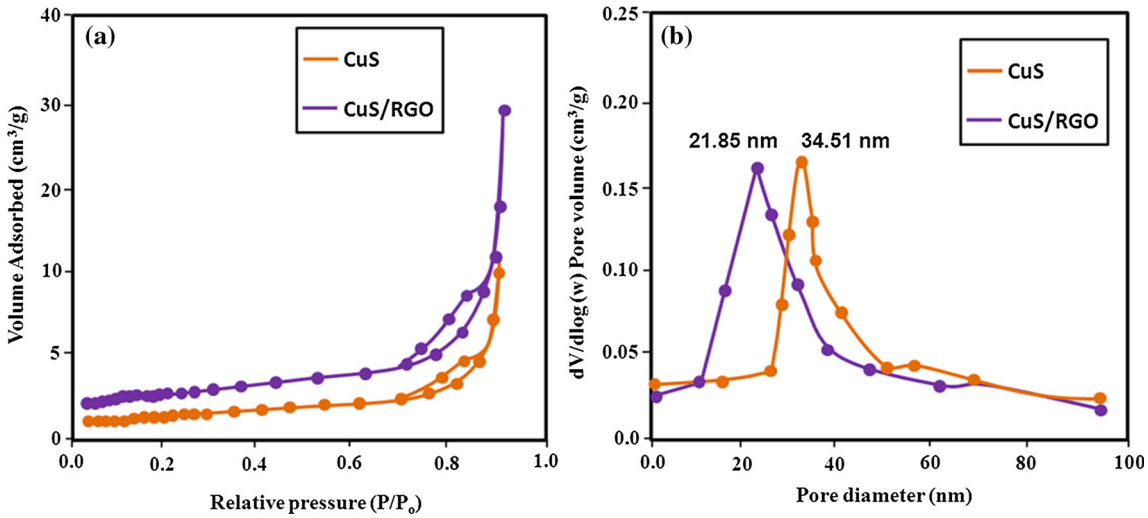

Fig. 6 **a** N_2 adsorption and desorption analysis pure CuS and CuS/RGO composite samples. **b** Corresponding pore size distribution

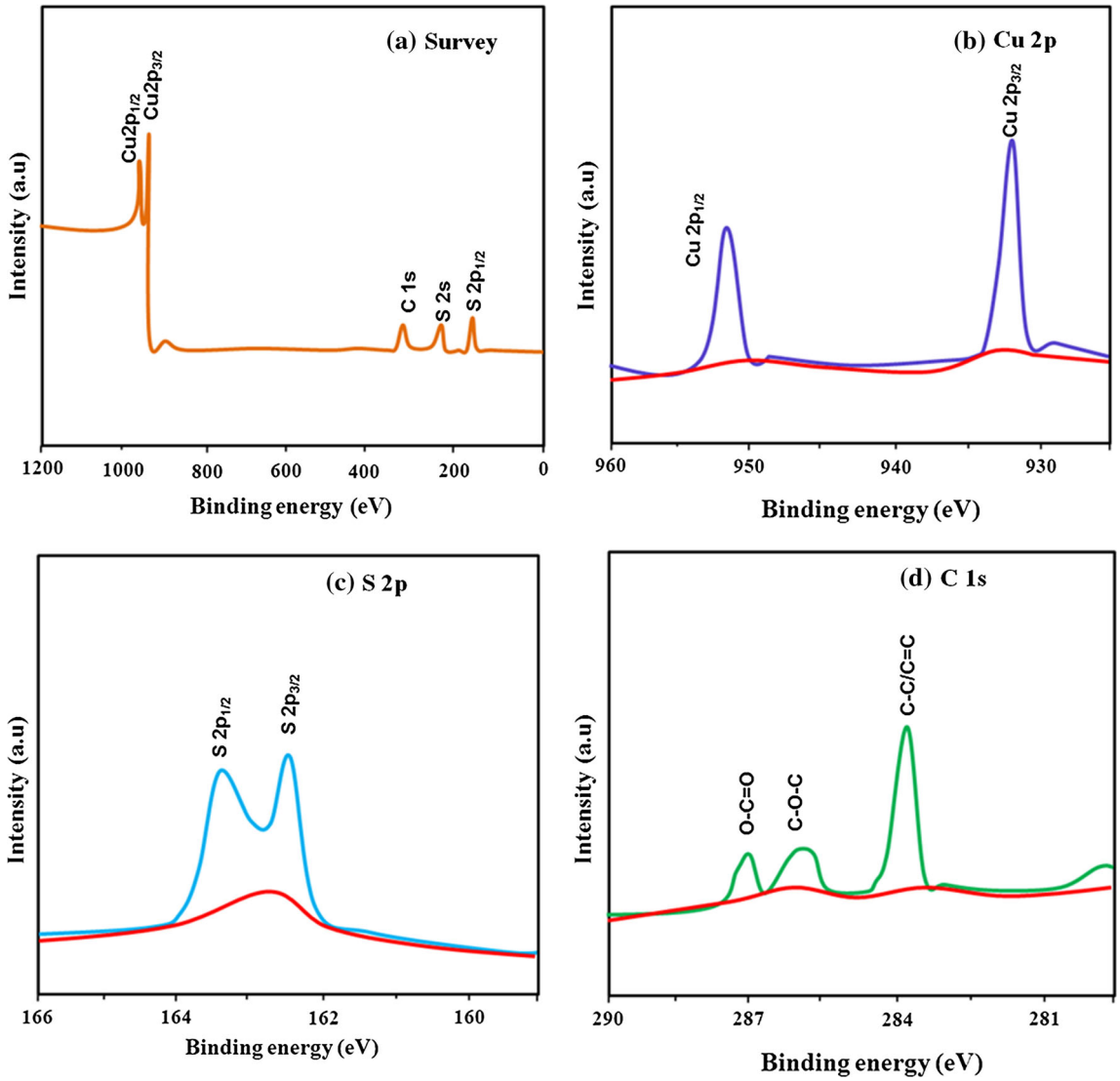

Fig. 7 XPS spectra of CuS/rGO **a** survey; **b** Cu 2p; **c** S 2p; and **d** C 1s

be 62.5 m^2/g and 21.85 nm respectively (Fig. 6b), which is higher than that of bare CuS (23.5 m^2/g and 34.51 nm). To further discover the valance state and elemental composition of the composite, XPS were recorded and the related graph is shown in Fig. 7. Figure 7a shows the wide range survey spectrum of the CuS/RGO composite sample, which is mainly composed of Cu, S and C elements. Figure 7b displayed the high resolution Cu 2p XPS spectra of the CuS/RGO sample. The binding energies at 932.8 and 952.7 eV correspond to $2p_{3/2}$ and $2p_{1/2}$ is belongs to Cu [33]. The high resolution spectrum (Fig. 7c) of S 2p shows the presence of S $2p_{3/2}$ and S $2p_{1/2}$ with relative binding energies of 162.4 and 163.3 eV respectively [34]. In C 1s region, the peaks located at 287.1, 286.3, and 283.7 eV can be assigned to O–C=O, C–O–C, and C–C/C=C, respectively (Fig. 7d). The photovoltaic cell was fabricated using CuS and CuS/rGO as photoanode and iodide/triiodide (I^-/I^{3-}) is used as an electrolyte and platinum (Pt) as the counter electrode. The schematic representation of sandwich type solar cell was shown in Fig. 8a. Ditetrabutylammonium *cis*-bis(isothiocyanato)bis(2,2-bipyridyl-4,4-dicarboxylato) ruthenium(II) (N719) dye was used to absorb the pure and composite samples. Iodide electrolyte containing I^-/I_3^- redox filled the space between the dye-sensitized photoelectrodes. When the DSSC was exposed to light, the photoexcitation occurred in the dye molecules, then the electron transferred from the highest occupied molecular orbital to the lowest molecular orbital states. The power conversion efficiency was calculated based on the previously published work [35]. Figure 8b shows the J–V characteristics curves of pure RGO, CuS and CuS/RGO nanocomposites were investigated under a simulated one

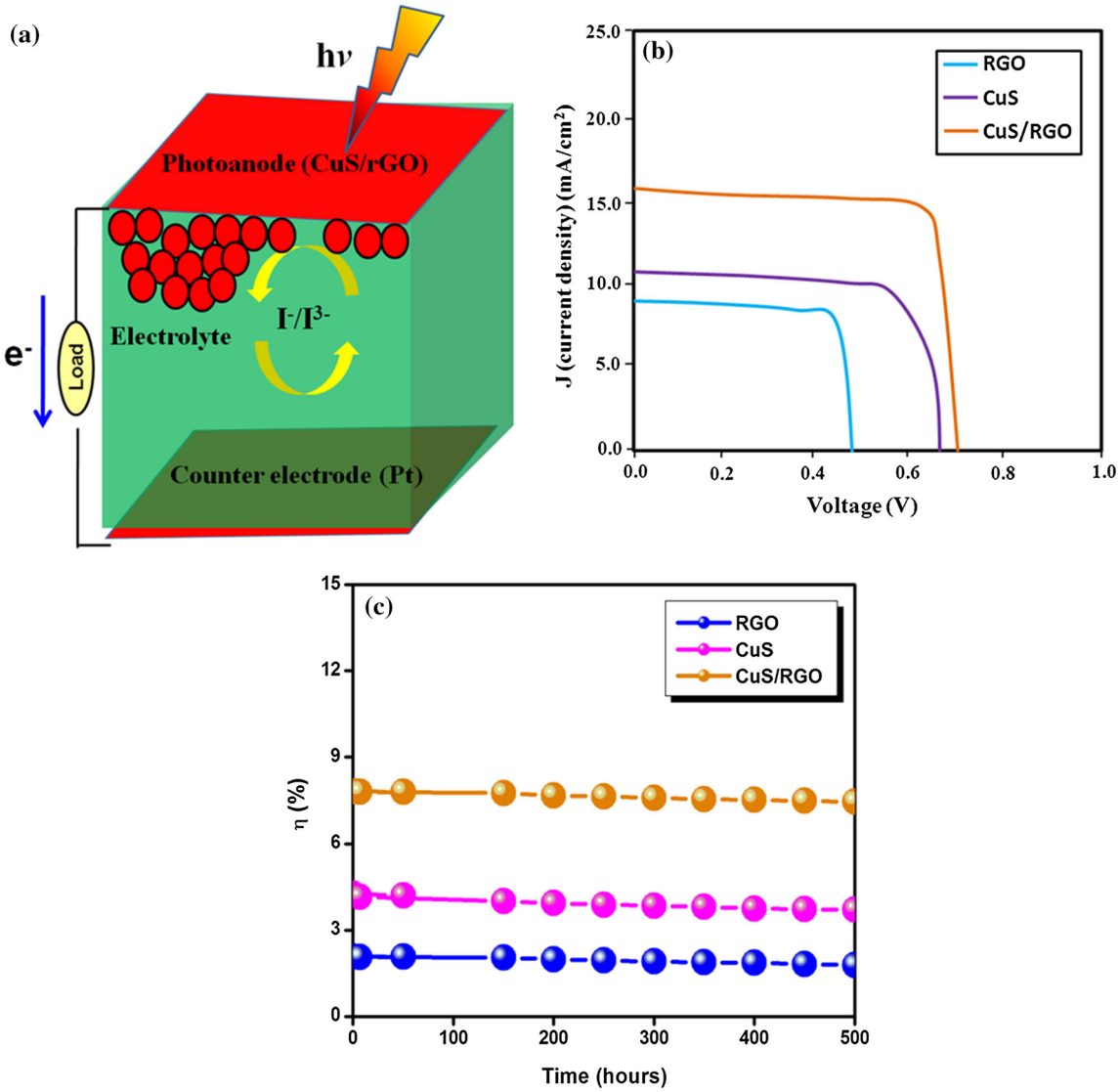

Fig. 8 **a** Schematic representation of the device; **b** photovoltaic performance of RGO, CuS and CuS/RGO composite samples and **c** stability test

Table 1 Photovoltaic parameters of pure RGO, CuS and CuS/RGO composite samples

Samples	Jsc (mA/cm^2)	Voc (V)	FF (%)	η (%)
RGO	9.2	0.48	48.1	2.08
CuS	11.1	0.64	56.1	4.27
CuS/RGO	16.0	0.71	70.1	7.81

sun solar irradiation of AM 1.5G, 100 mW/cm^2. The results demonstrate that CuS/RGO showed high PCE than other samples. The finest PCE was found to be 7.81% of CuS/RGO composite than compared with bare CuS (4.27%). The photocatalytic parameters were shown in Table 1. The stability curve of CuS and CuS/RGO is shown in Fig. 8c. The stability test was carried out under the same experimental condition with the extending light illumination up to 500 h. After 500 h of testing, the slight degradation was observed in the PCE from the initial value. The stability of PCE was found to be 85, 88 and 95% of RGO, CuS and CuS/RGO samples respectively. The results suggest that CuS/RGO composite CE have good stability and suggest that the CuS/RGO composite material could act as high efficient in photovoltaic devices.

Conclusions

This study explored the synthesis with a simple hydrothermal method of CuS/RGO nanocomposites with improved photovoltaic performance. XRD, XPS, Raman spectra, TEM and UV–Vis DRS showed the spherical shaped CuS NPs was extremely dispersed and anchored on the RGO nanosheets. The prepared CuS/RGO photoelectrode showed high photo conversion efficiency (7.81%) than bare CuS (2.08%). This could be due to RGO could efficiently separate the photoinduced charge carriers and holdup the recombination. The overall results suggest that the newly prepared CuS/RGO hybrid composite is one of promising flexible counter electrode for three generation solar cells due to its high efficiency, low cost and facile preparation method.

References

1. L. Suganthi and A. A. Samuel (2012). *Renew. Sustain. Energy. Rev.* **16**, 1223.
2. M. Z. Iqbal and S. Khan (2018). *Sol. Energy* **160**, 130.
3. J. Wu, Z. Lan, J. Lin, M. Huang, Y. Huang, L. Fan, G. Luo, Y. Lin, Y. Xie, and Y. Wei (2017). *Chem. Soc. Rev.* **46**, 5975.
4. M. S. Dresselhaus and I. L. Thomas (2001). *Nature* **414**, 332.
5. M. R. Narayan (2012). *Renew. Sustain. Energy Rev.* **16**, 208.
6. A. V. Shah, R. Platz, and H. Keppner (1995). *Sol. Energy Mater Solar Cells* **38**, 501.
7. A. Hagfeldt, G. Boschloo, L. Sun, L. Kloo, and H. Pettersson (2010). *Chem. Rev.* **110**, 6595.
8. M. Sumathi, A. Prakasam, and P. M. Anbarasan (2019). *J. Clust. Sci.* **30**, 757.
9. M. Yousefi, M. Sabet, M. Salavati-Niasari, and S. M. Hosseinpour-Mashkani (2012). *J. Clust. Sci.* **23**, 491.
10. M. Yousefi, M. Sabet, M. Salavati-Niasari, and H. Emadi (2012). *J. Clust. Sci.* **23**, 511.
11. M. Abdi-Jalebi, M. R. Mohammadi, and D. J. Fray (2014). *J. Clust. Sci.* **25**, 1029.
12. Z. Zarghami, M. Ramezani, and K. Motevalli (2016). *J. Clust. Sci.* **27**, 1451.
13. J. G. Radich, R. Dwyer, and P. V. J. Kamat (2011). *Phys. Chem. Lett.* **2**, 2453.
14. Z. Yang, C. Chen, C. Liu, C. Li, and H. Chang (2011). *Adv. Energy Mater.* **1**, 259.
15. Z. Yang, C. Chen, C. Liu, and H. Chang (2010). *Chem. Commun.* **46**, 5485.
16. Z. Tachan, M. Shalom, I. Hod, S. Ruhle, and S. Tirosh (2011). Zaban. *J. Phys. Chem. C* **115**, 6162.
17. J. Kundu, D. Pradhan, and A. C. S. Appl (2014). *Mater. Interfaces.* **6**, 1823.
18. X. Jiang, Y. Xie, J. Lu, W. He, L. Zhu, and Y. Qian (2010). *J. Mater. Chem.* **10**, 2193.
19. J. S. Chung and H. J. Sohn (2002). *J. Power Sources.* **108**, 226.
20. A. B. F. Martinson, J. W. Elam, and M. J. Pellin (2009). *Appl. Phys. Lett.* **94**, 123107.
21. M. Basu, A. K. Sinha, M. Pradnan, S. Sarkar, Y. Negishi, and T. Pal (2010). *Environ. Sci. Technol.* **44**, 6313.
22. S. Stankovich, D. A. Dikin, G. H. B. Dommett, K. M. Kohlhaas, E. J. Zimney, E. A. Stach, R. D. Piner, S. T. Nguyen, and R. S. Ruoff (2006). *Nature.* **442**, 282.
23. D. A. Brownson and C. E. Banks (2010). *Analyst.* **135**, 2768.
24. W. S. Hummers and R. E. Offeman (1958). *J. Am. Chem. Soc.* **80**, 1339.
25. S. Drewniak, R. Muzyka, A. Stolarczyk, T. Pustelny, M. Kotyczka-Morańska, and M. Setkiewicz (2016). *Sensors.* **16**, 103.
26. M. Parthibavarman, K. Vallalperuman, S. Sathishkumar, M. Durairaj, and K. Thavamani (2014). *J. Mater. Sci. Mater. Electron.* **25**, 730.
27. H. C. Tao, X. L. Yang, L. L. Zhang, and S. B. Ni (2014). *J. Phys. Chem. Solids.* **75**, 1205.
28. L. Fei, Q. L. Lin, B. Yuan, G. Chen, P. Xie, Y. L. Li, Y. Xu, S. G. Deng, S. Smirnov, and H. M. Luo (2013). *ACS Appl. Mater. Interfaces.* **5**, 5330.
29. M. Parthibavarman, S. Sathishkumar, M. Jayashree, and R. BoopathiRaja (2019). *J. Clust. Sci.* **30**, 351.
30. M. Parthibavarman, S. Sathishkumar, S. Prabhakaran, M. Jayashree, and R. BoopathiRaja (2018). *J. Iran. Chem. Soc.* **15**, 2789.
31. J. Zhou, F. Zhao, X. Wang, Z. Li, Y. Zhang, and L. Yang (2006). *J. Lumin.* **237**, 237.
32. X. S. Hu, Y. Shen, Y. T. Zhang, and J. J. Nie (2017). *J. Phys. Chem. Solid.* **103**, 201.
33. M. Saranya, R. Ramachandran, P. Kollu, S. K. Jeong, and A. N. Grace (2015). *RSC Adv.* **5**, 15831.
34. J. Zhao, D. Liu, C. Gu, M. Zhu, S. O. Ryu, and J. Huang (2018). *Mater. Chem. Phys.* **217**, 102.
35. Z. Li, F. Gong, G. Zhou, and Z. S. Wang (2013). *J. Phys. Chem. C.* **117**, 6561.